



# Weld Zone Characterization of Dissimilar SS UNS S43000/ UNS S32304 Joined through Laser Beam Welding: EBSD Study, Phase Evolutions, and Fractography

Hossein Mostaan, Morteza Shmanian, Reza Moradi, Fardin Nematzadeh, Ali Sonboli, and Jerzy A. Szipunar

Submitted: 22 May 2020 / Revised: 4 August 2020 / Accepted: 5 September 2020 / Published online: 27 October 2020

Dissimilar joints are growingly prevailing modern design of a wide range of equipment, especially in petrochemical, oil, and gas industries. In this research, UNS 43000 ferritic stainless steel and UNS 32304 duplex stainless steel were welded by a laser beam welding process in butt joint configuration, and microstructural evolutions and phase formation during laser welding were investigated using electron backscatter diffraction. The effect of heat input on the tensile properties and fracture behavior of the welded joint was also studied. It was observed that irregular grain orientations implied a relatively weak texture in the laser-welded joint. It was also found that three different phases, i.e.,  $\alpha$  (with bcc crystal structure),  $\gamma$  (with fcc crystal structure), and  $\text{Cr}_7\text{C}_3$  (with hcp crystal structure), appeared in different areas of the welded joint. The predominant phase in the welded metal and the heat-affected zone was  $\alpha$  (bcc). Also, despite the concentrated heat source on laser beam welding and the associated short cooling times, no martensitic structure was formed in these areas. By moving toward UNS 32304 base metal, more  $\gamma$  (fcc) phase was formed in the welded metal, which could be attributed to the higher concentration of austenite stabilizer elements, e.g., Ni and N, at UNS 32304 side. The presence of distinguished forms of austenite with fcc crystal structure, namely grain boundary allotriomorphic austenite and wedge-shaped Widmanstätten austenite, was seen mainly at ferrite grain boundaries and ferrite grain interior, respectively.

**Keywords** dissimilar welding, EBSD, laser welding, UNS S43000, UNS S32304

## 1. Introduction

Ferritic stainless steel containing 10–30% of chromium in solid solution along with other alloying elements (with or without nickel) has excellent properties, such as high resistance to stress corrosion cracking and high pitting resistance, especially in chloride media (Ref. 1–5). It is also less expensive as it contains no nickel. The ferritic stainless steel has a great advantage—i.e., lower expansion coefficient—over austenitic stainless steel, so it can be used in applications in which resistance to temperature cycling is necessary (Ref. 3, 6). Also, ferritic stainless steel has found some important applications such as in the upstream part of exhaust lines, coal carriages, mufflers, and catalytic converters (Ref. 3, 7, 8). On the other side, duplex (dual-phase) stainless steel contains austenite ( $\gamma$ ) and ferrite ( $\alpha$ ) phases in its microstructure designed to represent an outstanding combination of beneficial aspects of austenitic and ferritic stainless steel, so they have generally high strength

and stress resistance against stress corrosion cracking (Ref. 5, 9–11). The recent emergence of advanced stainless steel, such as duplex stainless steel, is basically related to the soaring of the nickel prices in recent years (Ref. 12).

UNS 32304 duplex stainless steel contains both austenite and ferrite phases in an equal proportion and shows enhanced toughness due to the austenite phase and an increased yield strength owing to the presence of ferrite phase in its structure. Consequently, duplex stainless steel is a good candidate for applications in some industries, such as nuclear power generation, heat exchangers, petrochemical equipment, subsea equipment, or other types of applications that are working in tough corrosive environments (Ref. 5). The selection of advanced duplex stainless steel is to meet an essential need to address the issue of dissimilar joining of metallic alloys. The welding of dissimilar metallic alloys (bimetallic joints), especially between ferritic and austenitic stainless steel, is relatively common in a broad range of applications due to their specific mechanical and physical performance characteristics, which enable us to exploit the advantages of both metals. Other motivations for joining dissimilar alloys are reducing manufacturing costs and increasing flexibility in design and application (Ref. 13, 14). These applications include parts of boilers subjected to a relatively lower temperature and also central power stations (Ref. 14).

However, dissimilar welding of alloys with different physical properties such as melting point and expansion coefficient has its own challenges (Ref. 13, 15). During dissimilar fusion welding between two different stainless steel pieces, the two base metals experience a severe thermal history which deteriorates the performance of the joint area including pitting resistance, toughness, and ductility. The degradation of joint properties arises from the precipitation of undesired

**Hossein Mostaan, Reza Moradi, Fardin Nematzadeh, and Ali Sonboli**, Faculty of Engineering, Department of Materials and Metallurgical Engineering, Arak University, Arak 38156-8-8349, Iran; **Morteza Shmanian**, Department of Materials Engineering, Isfahan University of Technology, Isfahan 84156-83111, Iran; and **Jerzy A. Szipunar**, Department of Mechanical Engineering, University of Saskatchewan, Saskatoon, SK S7N 5A9, Canada. Contact e-mail: H-mostaan@araku.ac.ir.

phases such as sigma, chi, and chromium carbide, the presence of excessive ferrite phase, grain growth, and so on (Ref. 16). The major problem in ferritic stainless steel would be the abnormal grain growth in the heat-affected zone (HAZ), which reduces toughness, while the ferritization of HAZ and weld metal (WM) is considered a major subject in fusion welding of duplex stainless steel, which causes a reduction in corrosion resistance (Ref. 3, 17, 18). In fact, grain coarsening and the formation of sigma phase in the HAZ of ferritic stainless steels can be hindered by applying a solid-state welding process or a low heat input process, such as laser beam welding, electron beam welding, and resistance spot welding (Ref. 19, 20). Researchers suggest that the ferritization of HAZ during fusion welding of duplex stainless steel is caused by the solidification of these alloys. A delta ferrite and the two-phase austenitic microstructure evolve during the phase transformation in the solid-state (Ref. 21). The formation of excessive ferrite phase in the HAZ of duplex stainless steel is even more promoted during a laser welding process in which the cooling rate is very high (Ref. 22). Accordingly, it is of primer importance to obtain a desired microstructure that contains convenient phases and cannot be easily obtained even using low heat input and an advanced process, such as laser welding.

The advantages of laser beam welding include precise energy control, flexibility and repeatability, low thermal distortion, narrow HAZ, and high welding speed (Ref. 23). So, it is essential to comprehensively study phase transformation and microstructural evolutions during dissimilar fusion welding of duplex and ferritic stainless steel pieces. A great number of industrial applications, especially marine and chemical equipment, utilize the welding process as the primary way to form dissimilar bonding between duplex and ferritic stainless steel. The authors found very few or no research reports in the literature on the laser welding of thin duplex and ferritic stainless steel sheets. Using phase analysis techniques such as electron backscattered diffraction (EBSD), quantitative analysis can be performed on the welded joint to explore phase transformations and microstructural evolutions (Ref. 24). In the present work, the laser beam welding process was successfully employed to join UNS 32304 and UNS 43000 stainless steel pieces to obtain a sound and defect-free welded joint. Hence, the main goal of the present work was to investigate the microstructural evolutions and phase transformations in differ-

ent areas of UNS43000/UNS32304 dissimilar laser-welded joint by the means of the EBSD technique. The novelty of the research lies in investigating phase transition and secondary phase formation and in distinguishing the morphology of various phases formed in different welding areas.

## 2. Materials and Experimental Procedures

The butt joints were made of duplex 2304 type steel (UNS 32304) and 430 (UNS 43000) stainless steel. Two base materials with a size of  $50 \times 100 \times 1 \text{ mm}^3$  were used in the study. The chemical compositions of the as-received stainless steel pieces and the properties determined by the tensile test are listed in Tables 1 and 2, respectively. The standard tensile test was performed according to the ASTM E8M to evaluate the mechanical properties of the base materials and the welded samples. Three tensile specimens with the axis oriented perpendicular to the rolling direction were prepared from each welded sample. The tensile tests were performed at a strain rate of  $0.5 \text{ S}^{-1}$  on a Santam servo-hydraulic testing machine. A typical welded sample was etched with a commercial reagent (1 mg of picric acid, 5 ml of HCl, and 100 ml of ethanol) to reveal the microstructures (according to ASTM E 407-2015). The microstructures of the welded area were analyzed using an OLYMPUS GX50 optical microscope. Also, the parent materials were surface cleaned with sandpaper and acetone to remove any surface contaminations such as oxides, oil, and grease before welding.

The laser welding process was performed using a 280 W automatic welding machine with a disk laser of Nd: YAG. No filler was applied during laser welding. A flow rate of about 25 Lit/min of pure argon gas was used to avoid any undesired reaction between the weld pool and the surrounded air. The welding parameters are presented in Table 3. Electron backscattered diffractometry was done using a Hitachi scanning electron microscope (SEM) equipped with an energy dispersive spectroscopy (EDS). The specimen preparation method for the EBSD study was described in our previous work (Ref. 25). The analysis of the related EBSD results, data visualization, and post-processing was carried out using the ATEX software.

**Table 1 The chemical composition of the applied base materials**

Element, wt.%	C	Cr	Mn	Ni	N	Si	S	P	Fe
UNS 32304	0.03	22.5	1.85	4.3	0.12	1.1	0.013	0.032	Bal.
UNS 43000	0.11	11	0.89	...	...	0.92	0.028	0.029	Bal.

**Table 2 The mechanical properties of the studied base materials**

Properties	Tensile strength, MPa	Yield strength, MPa	Elongation, %
UNS 32304	641	400	25
UNS 43000	535	410	29

**Table 3** The laser welding parameters for joining UNS 32304 and UNS 43000 stainless steel pieces

Parameter	Description
Laser type	Pulsed Nd: YAG
Wavelength	1064 nm
Pulse Frequency	10 Hz
Focal length	100 mm
Laser spot size	100 $\mu\text{m}$

**Table 4** The laser beam welding parameters for each sample

Parameter	Welding speed, mm/min	Peak power, kW	Defocusing distance, mm
Sample A (low heat input)	5	1.2	1
Sample B (medium heat input)	1	1.2	1
Sample C (high heat input)	1	2.7	1

### 3. Results and Discussion

To investigate the effects of heat input on the microstructure and fracture behavior of the joints, three typical samples with different welding parameters were welded using an ND: YAG welding machine. The parameters recorded for each sample are shown in Table 4. The formula used to calculate heat input is as follows:

$$\text{Heat input} = \frac{\text{Pulse energy}(E_p) \times \text{Pulse frequency}(f)}{\text{Travel Speed}} \quad (\text{Eq 1})$$

A series of preliminary experiments were conducted to achieve a sound and defect-free weld interface with a smooth weld bead. The welding current, defocusing distance, and beam power were considered as the main effective parameters.

A typical low magnification macrograph showing the weld bead geometry and also high magnification SEM micrographs of the base metals (BM) are illustrated in Fig. 1.

The cross section of the welded joint exhibits a V shape with narrow HAZ (Fig. 1a), which results from the high cooling rates and low heat input during laser welding. This process was typically conducted at high welding speeds. No concavity or convexity was observed in the face or root of the welds. Also, no visible cracking or porosity was found within the weld. So, a

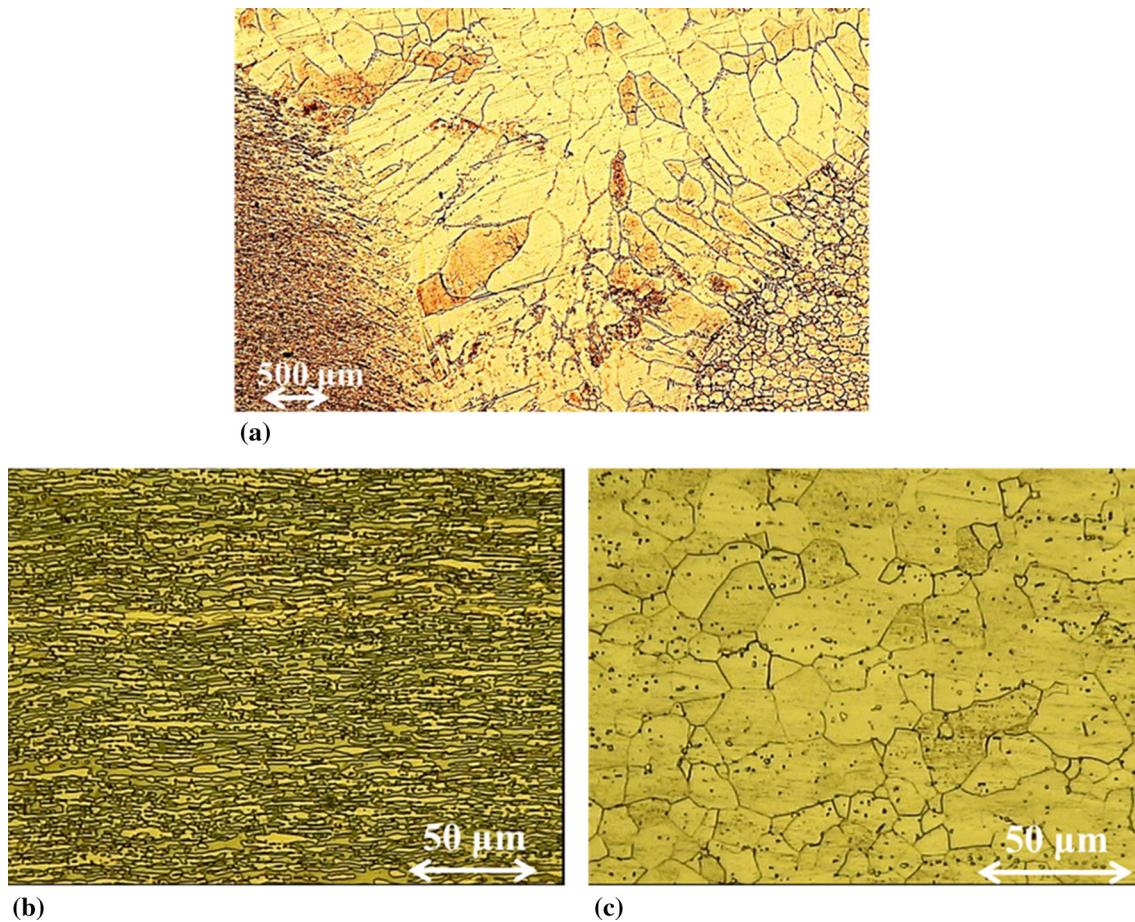


**Fig. 1** The OM micrographs from (a) the cross section of the typical welded sample, (b) the UNS 32304 BM, and (c) the UNS 43000 BM



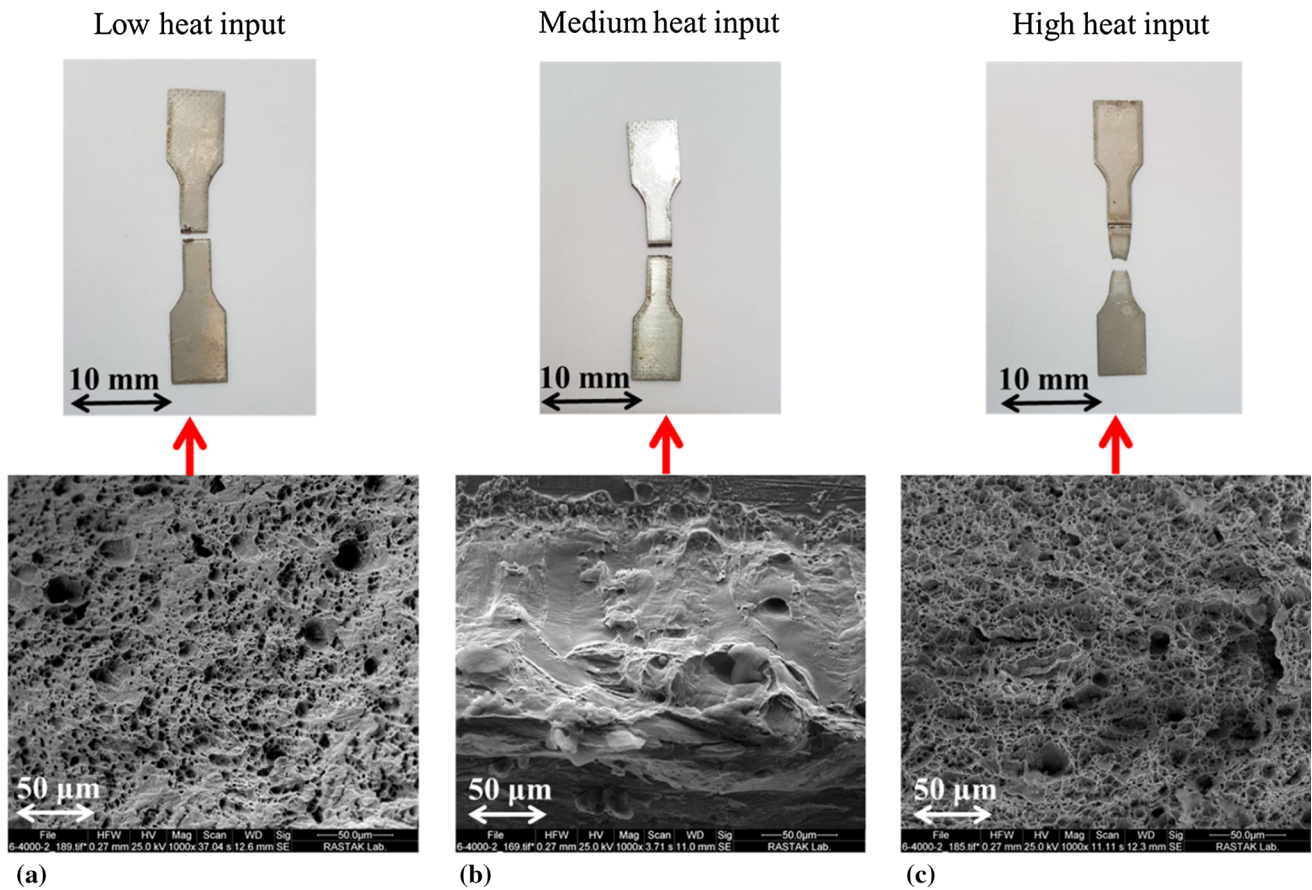


**Fig. 2** SEM images from the fracture surfaces in the SE mode: (a) low heat input, (b) medium heat input, and (c) high heat input

sound defect-free weld shape can be achieved by autogenous laser welding. The microstructure of UNS 43000 BM is shown in Fig. 1(c). This BM was in the cold-rolled + annealed conditions. So, the microstructure of the UNS 43000 BM is fully ferritic, and some carbides (majorly  $M_{23}C_6$ ) can be found in the BM microstructure which are uniformly distributed throughout the matrix. Figure 1(a) exhibits the typical optical microstructures of BM for UNS 32304 in a solutionized condition. As can be seen, this micrograph consists of bright  $\gamma$ -islands embedded in the darker  $\alpha$ -ferrite matrix or in the boundaries of ferrite. Also, no secondary precipitate can be seen in the microstructure. The analysis of the micrograph showed that the ferrite phase fraction was about 48.5%.

To evaluate the fracture behavior of the welded samples with different welding parameters, the fracture surfaces were investigated by SEM.

The tensile strength of the samples welded by low, medium, and high heat inputs was 522, 360, and 468 MPa, respectively. A close examination of the topography and fracture features can help to determine the fracture mode and determine the fracture origin and crack direction. Figure 2 depicts the SEM images from the fracture surfaces of each sample. Moreover, the images from the test samples after the tensile test are shown in this figure. It is clear from the images that the samples with low and medium heat input were fractured in the weld zone, and the sample welded with maximum heat input was fractured in the UNS 43000 BM. This indicates that the low and medium heat input samples had lower strength values than that of the BM, and the high heat input sample (sample C) had a higher

strength. The failure of the samples with low or medium heat inputs from the weld area during the tensile test is mainly due to the incomplete penetration of the weld metal, which increases stress concentration (see Fig. 3). The high heat input sample has full penetration and hence shows a higher strength than the BM. It should be noted that the tensile strength of UNS 32304 is higher than that of UNS 43000, and UNS 43000 is expected to fail. As shown in Fig. 2(c) for the high heat input sample, the fracture face is considerably smaller than the original cross-sectional area because of a significant reduction in area and high ductility of the UNS 43000 BM before fracturing. No noticeable elongation can be observed in the low and medium heat inputs. On the other hand, this is well noticed in the fractography results that the low heat input sample (Fig. 2a) showed an approximately ductile fracture. This failure mechanism observed in this welded sample is microvoid coalescence (MVC), which is associated with ductile failure. This is obvious by the major part of the fracture surface containing a dimpled feature. During this fracture mode, as the strain increased in the microstructure, microvoids nucleated at local strain concentrations, such as second phase particles, inclusions, grain boundaries, and dislocation pileups. The microvoids grew and eventually coalesced to form a continuous network of cup-like dimples.

The fracture surface morphology of the sample welded with medium heat input (sample B) is shown in Fig. 2(b). This image indicates that the fracture in this sample occurred in a brittle mode owing to the smoothness and featurelessness of the fracture surface. In other words, in this sample, a transgranular



cleavage fracture occurred which was caused by the impact of overload in the welded area. This is a low energy fracture that tends to propagate transgranularly. The brittle fracture of the sample B in comparison with the sample A can be attributed to the higher heat input on the sample B and the resulting slower cooling rate in this sample. During the slow cooling of the weld metal, more brittle carbides can be formed at favorable sites, such as grain boundaries. These second phases may result in a brittle fracture. According to Lee et al. (Ref. 26), the presence of coarse carbide, particularly  $M_3C$  and  $M_{23}C_6$ , causes the formation of microcracks which are propagated in the ferrite matrix. In the following paragraphs, the nature of the carbides in the fusion zone is comprehensively discussed.

Since it is not easy to identify the microstructural and phase evolutions only through the SEM method, the EBSD technology can be utilized to provide a quantitative tool to study microstructures in large scales (Ref. 27).

Hence, the EBSD analysis was conducted to further study the microstructure. The application of EBSD facilitates distinguishing between the microstructure of the WM, HAZ, and BM microconstituents and microtexture. The inverse pole figure (IPF) shows the texture of the microstructure in a specified zone. To provide fundamental insight into the grain structure development, a large EBSD map was developed for a typical welded joint (taken from the UNS 43000 BM to UNS 32304) as shown in Fig. 4.

An overview of the butt joint cross sections reveals clear differences in grain size. Independent of the welding conditions, the WM exhibits a coarser solidification microstructure typical for the fusion welding process. When the molten pool

was solidified, equiaxed grains with random orientations were produced in the welded metal. Also, the irregular grain orientations implied a relatively weak texture in the laser-welded joint. More investigations showed that only three different phases, i.e.,  $\alpha$  (with bcc crystal structure),  $\gamma$  (with fcc crystal structure), and  $Cr_7C_3$  (with hcp crystal structure), appeared in different areas of the welded joint. The formation of these phases is discussed below in more detail. Also, the absence of any solidification cracks in the WM confirmed that laser welding with the process parameters and complete mixing of alloying elements was effective.

To study the microstructural changes and phase evolutions during laser welding of UNS 43000 and UNS 32304, the EBSD analysis was performed on each side in more detail. The EBSD maps from UNS 43000 side representing the bcc phase are shown in Fig. 5, and some selected subareas (HAZ and BM) are given at higher magnifications. As can be seen in these figures, the predominant phase in the WM, HAZ, and UNS 43000 was  $\alpha$  (bcc). Also, despite the concentrated heat source on laser beam welding and the associated short cooling times, no martensitic structure was formed in the WM as well as in the HAZ. It has been reported by some researchers that some martensite phase is formed in the grain boundaries of ferritic grains. But, it seems that due to the presence of some austenite stabilizer elements, e.g., N and Ni, in the welded metal, the martensite phase could not be formed even in such a high cooling rate. Under high cooling rates in laser or electron beam welding, a weld metal is solidified as primarily  $\delta$ -ferrite when the  $Cr_{eq}$  to  $Ni_{eq}$  ratio is higher than 1.7. According to the

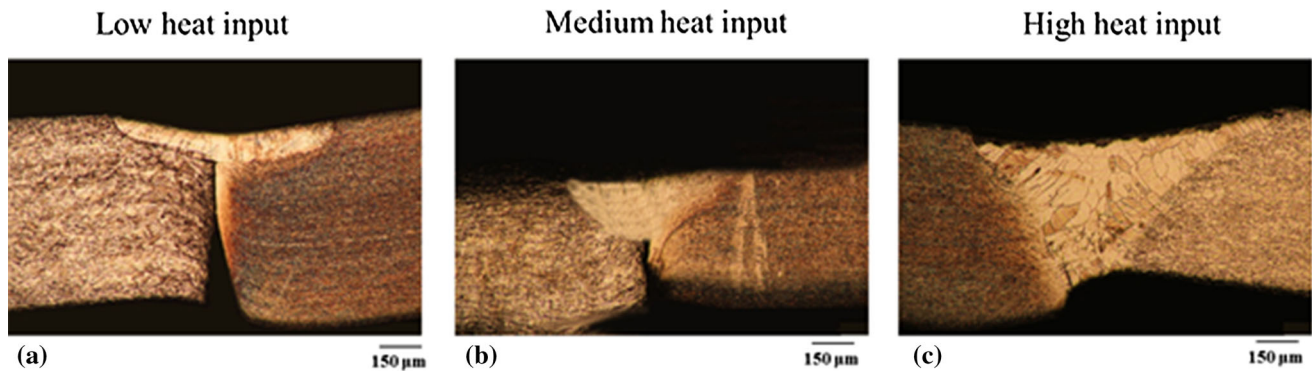


Fig. 3 Optical macrographs from the cross section of the welded joints in different conditions

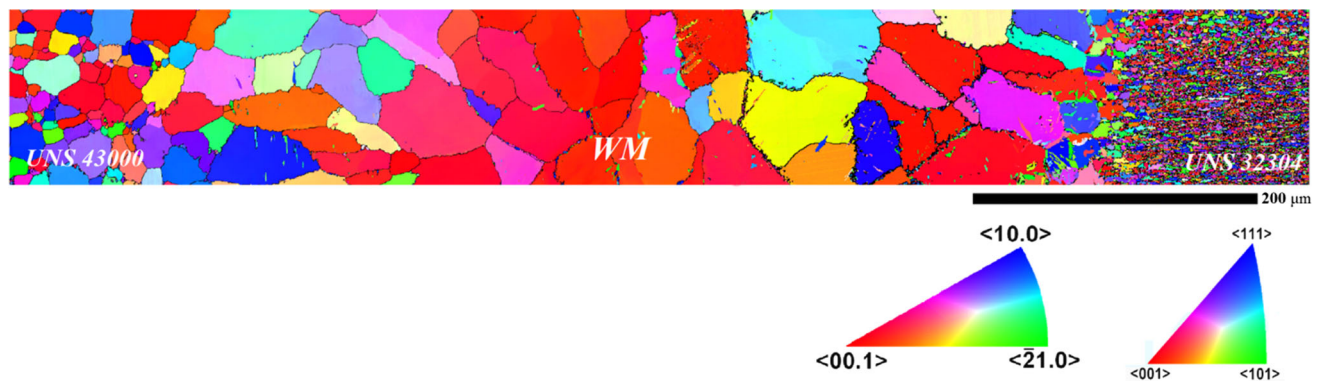


Fig. 4 A high-resolution EBSD image from a typical welded joint between UNS 43000 and UNS 32304

chemical composition of the UNS 43000 and UNS 32304 BMs and based on Eqs. 2 and 3, this ratio is about 3.7.

$$Cr_{eq} = \%Cr + \%Mo + 1.5\%Si + 0.5\%Nb + 2\%Ti \quad (\text{Eq 2})$$

$$Ni_{eq} = \%Ni + 30\%C + 0.5\%Mn \quad (\text{Eq 3})$$

Accordingly,  $\delta$ -ferrite is the first phase to solidify followed by some transformation from  $\delta$ -ferrite into austenite during cooling. Further, cooling leads to the transformation of the austenite phase into  $\alpha$ -ferrite and Cr-rich carbides. As is evident, no  $\delta$ -ferrite remains in the WM. The analysis shows that the grains in the HAZ have a mean size of about 38  $\mu\text{m}$  and have no preferred orientation compared to BM and WM.

The EBSD maps from the UNS 43000 side representing the  $\gamma$  (fcc) phase are shown in Fig. 6, and some selected subareas (HAZ and BM) are given at higher magnifications. As it can be seen in this figure, almost no phase with the fcc crystal structure is present in the UNS 43000 BM and its HAZ, while some few sporadic  $\gamma$  (fcc) phase is observed in the WM (near the HAZ). By moving toward the UNS 32304 BM, more  $\gamma$  (fcc) phase is seen in the WM. This can be attributed to the higher concentration of the austenite stabilizer element such as Ni and N at the UNS 32304 side.

The EBSD maps from the UNS 43000 side representing the  $Cr_7C_3$  phase with hcp structure are displayed in Fig. 7. This figure illustrates that the Cr-rich  $M_7C_3$  carbides are the dominant precipitates, distributing mainly along the grain boundaries and inside the grains (in WM). It has been shown that the chromium-rich carbides primarily precipitate in unstabilized ferritic stainless steels such as UNS 43000. As reported by other researchers (Ref. 18, 28), it is opined that severe mixing of UNS 43000 in the WM enhances the carbon content in the weld area leads to nucleate carbide intermetallic.

Also, it was found from the EBSD analysis that there are no intermetallic compound phases, i.e.,  $\chi$  and  $\sigma$ , in the welded joint. High heat input fusion welding of these alloys leads to the formation of  $\chi$  and  $\sigma$  phases, resulting in low ductility and toughness.

The EBSD maps from the UNS 32304 side representing bcc phase are shown in Fig. 8 in which some selected subareas (HAZ and BM) are given at higher magnifications.

As can be seen, especially in the grain boundaries, a large amount of austenite phase was transformed into the  $\alpha$ -ferrite phase in the HAZ and thus the dominant phase in this zone would have a bcc crystal structure. The microstructure of the WM near the HAZ mainly consisted of  $\alpha$ -ferrite (even higher than that of in the HAZ) too.

The EBSD maps from the UNS 32304 side representing the  $\gamma$  (fcc) phase are shown in Fig. 9.

Changes in austenite morphology in the HAZ and WM are obvious. Also, a considerably lower content of austenite phase is formed in the WM which can be due to the higher temperature gradient in comparison with the HAZ. The presence of a distinguished form of austenite with an fcc crystal structure, i.e., grain boundary allotriomorphic austenite and wedge-shaped Widmanstätten austenite, is mainly seen at the ferrite grain boundaries and ferrite grain interior, respectively. Austenite is formed in a solid-state by nucleation and growth process, usually resulting in complete coverage of the ferrite grain boundaries by austenite depending on the process parameters. The phase equilibrium of ferrite and austenite strongly depends on the heat inputs, cooling rates, and the diffusion of the alloying elements. It has been shown that at higher  $Cr_{eq}$  to  $Ni_{eq}$  ratios (e.g., in this case), the microstructure would consist of ferrite matrix with grain boundaries and Widmanstätten austenite plates that nucleate at the grain boundary austenite or within the ferrite grains (Ref. 21). This

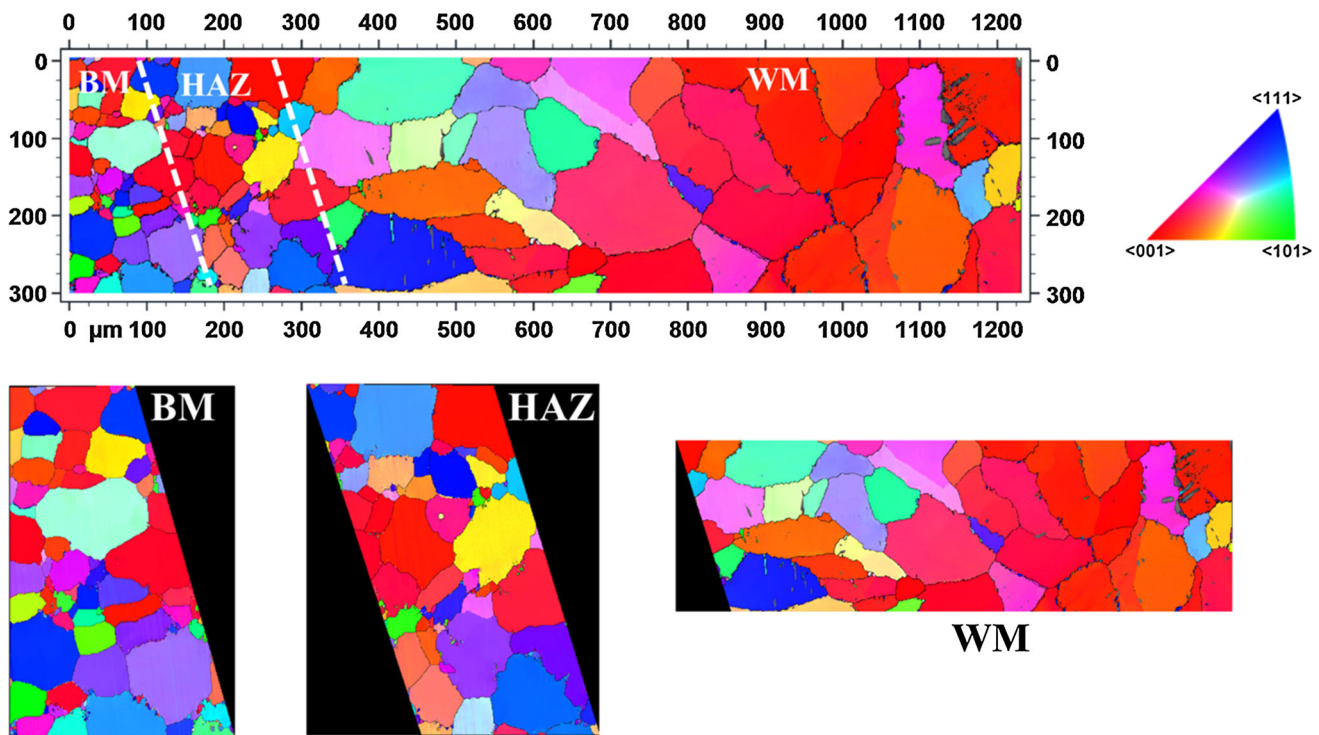
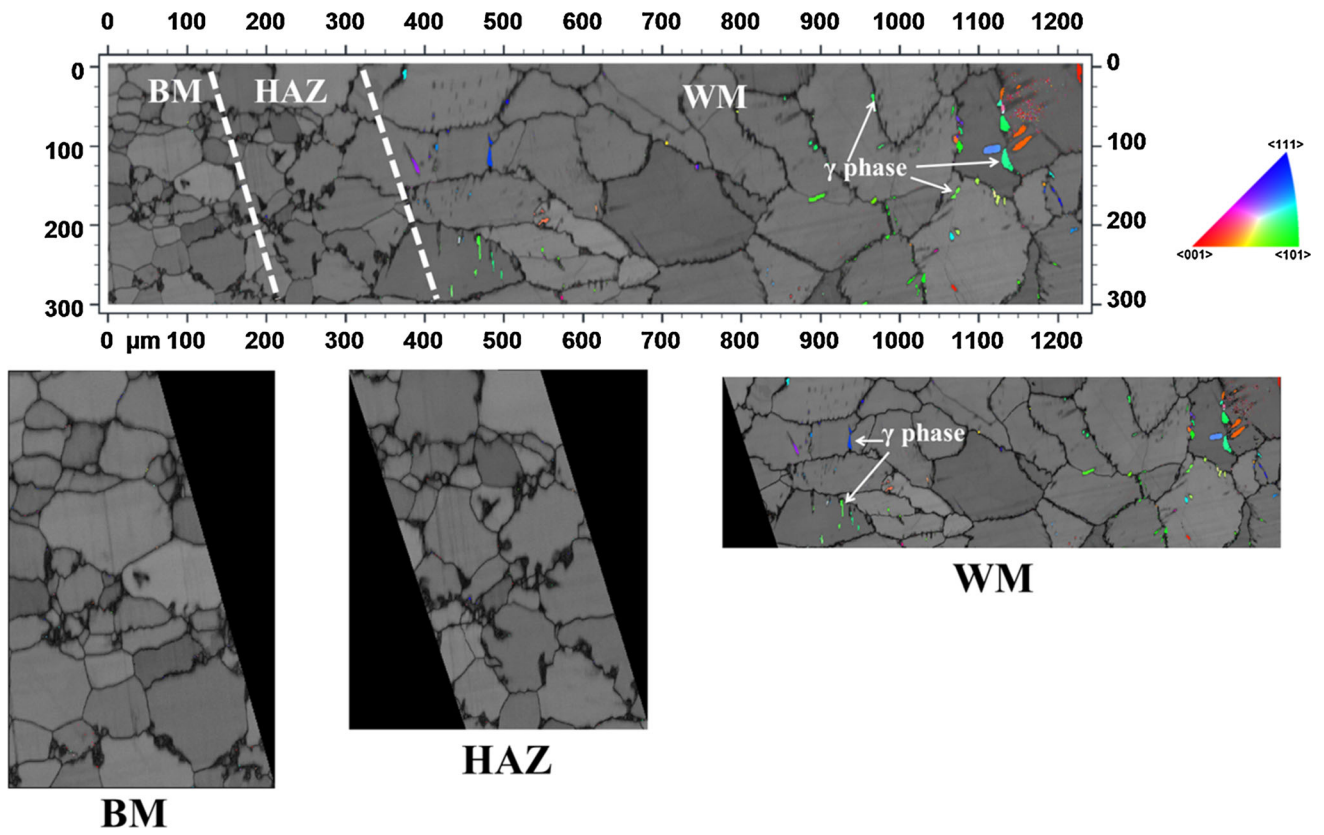
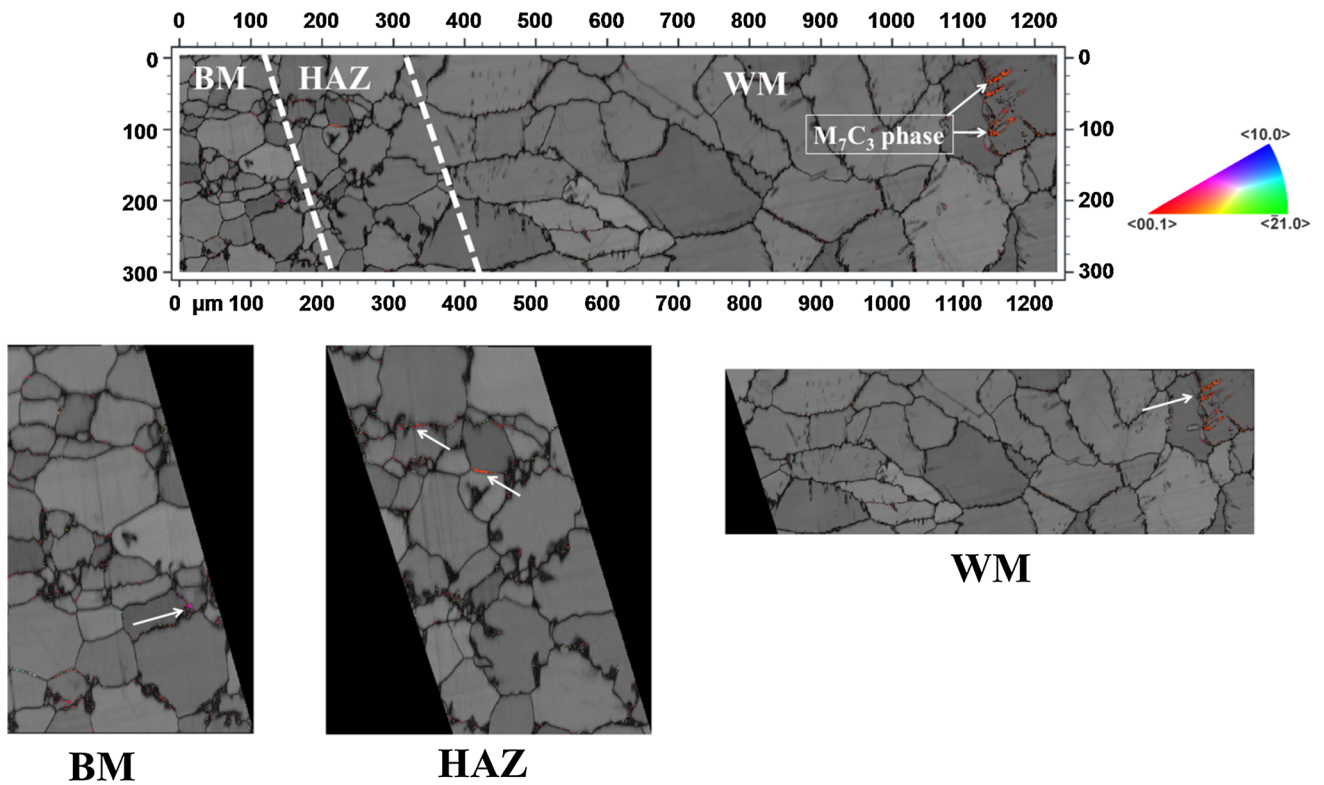


Fig. 5 The EBSD inverse pole figure mapping of the welded joint (from the UNS 43000 side) for  $\alpha$  phase



**Fig. 6** The EBSD inverse pole figure mapping of the welded joint (from the UNS 43000 side) for the  $\gamma$  (fcc) phase



**Fig. 7** The EBSD inverse pole figure mapping of the welded joint (from the UNS 43000 side) for the  $M_7C_3$  phase (hcp crystal structure)



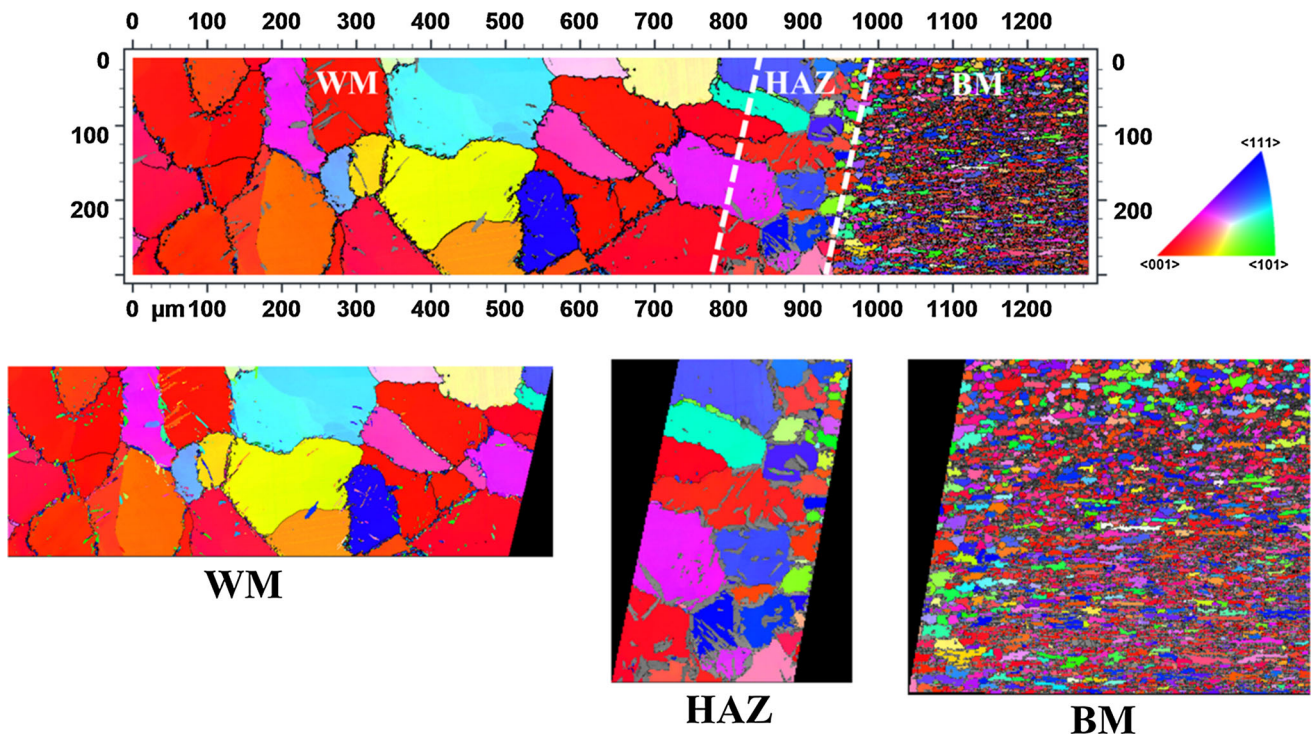


**Fig. 8** The EBSD inverse pole figure mapping of the welded joint (from the UNS 32304 side) for the  $\alpha$ -ferrite phase (bcc crystal structure)

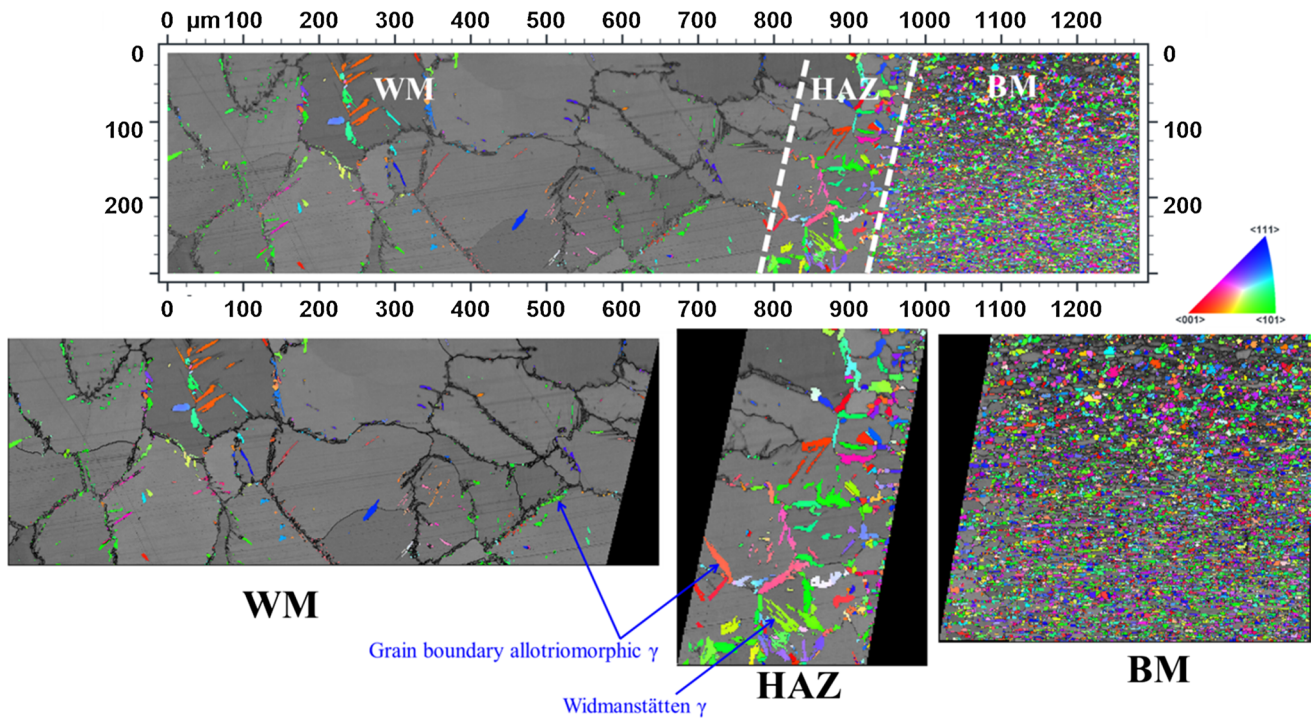


**Fig. 9** The EBSD inverse pole figure mapping of the welded joint (from the UNS 32304 side) for the  $\gamma$ -austenite phase (fcc crystal structure)

microstructure can be clearly seen in Fig. 9. In this case, transformation does not occur entirely across the ferrite grain. Initial austenite grain is suppressed by lower diffusion rates and a lower driving force. With an increase in the  $\text{Cr}_{\text{eq}}$  to  $\text{Ni}_{\text{eq}}$  ratio, the ferrite solvus decreases, and the ferrite content increases, reducing the driving force for the ferrite to austenite transformation and the temperature at which the transformation begins.

During the transformation, austenite begins to precipitate at  $\alpha/\alpha$  grain boundaries named as grain boundary austenite, whereas the Widmanstätten austenite nucleates from the grain boundary austenite in the direction of the grain.

The EBSD maps from the UNS 32304 side representing the Cr-rich  $\text{M}_7\text{C}_3$  phase with hcp structure are shown in Fig. 10.

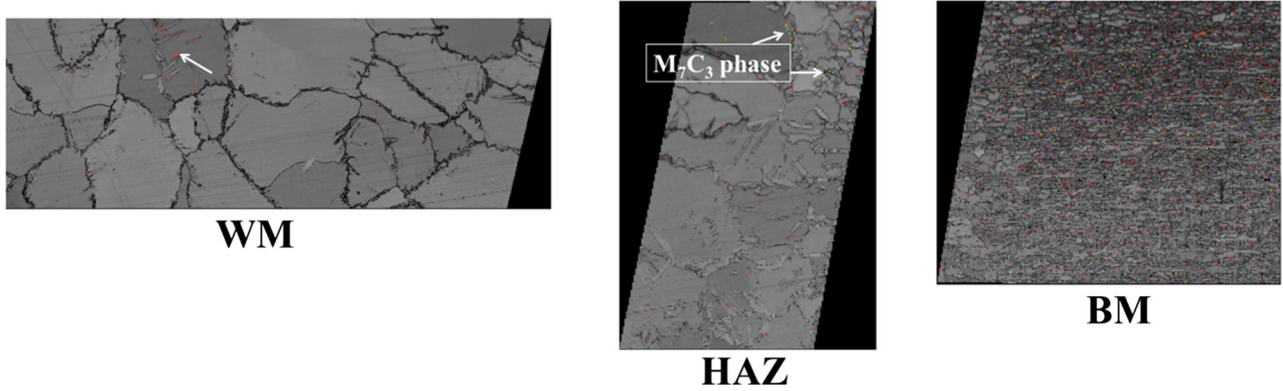
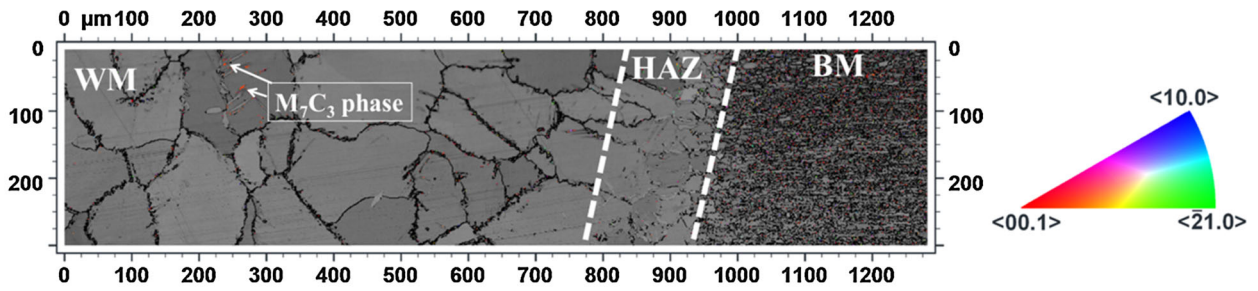


**Fig. 10** The EBSD inverse pole figure mapping of the welded joint (from the UNS 32304 side) for the  $\text{Cr}_7\text{C}_3$  phase (hcp crystal structure)

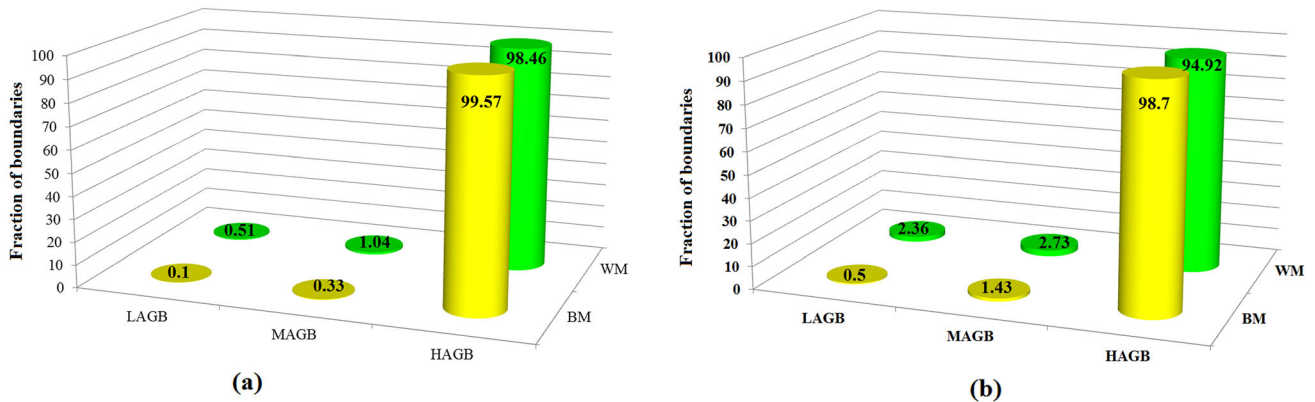


**Fig. 11** The fraction of high-, mean- and low-angle boundaries based on the EBSD analysis: (a) on the UNS 43000 and (b) on the UNS 32304

As can be seen in Fig. 10, there is only Cr-rich  $\text{M}_7\text{C}_3$  carbide in the HAZ and WM (near the HAZ). In this study, it was observed that no nitride phase was formed in the HAZ or WM, which is in contradiction with the earlier results reported by other researchers (Ref. 5, 29).

The changes in the densities of low-angle grain boundaries, mean-angle grain boundaries, and high-angle grain boundaries during laser welding between UNS 43000 and UNS 32304 are displayed in Fig. 11 (see also Fig. 12).

The fraction of the rotation angle ( $\theta < 5^\circ$ ) reflects the percentage of low-angle grain boundaries (LAGB) whose density depends on the misorientation angle. This type of boundaries is the aggregation of dislocation that contains dislocation elastic energy. The rotation angle  $\theta$  of greater than  $15^\circ$ , which contains some layers of atoms, reflects the proportion of grain boundaries known as high-angle grain boundaries (HAGB). The boundaries with a rotation angle of

$5^\circ$ - $15^\circ$  are known as mean-angle grain boundaries (MAGB). The analysis of data showed that the relative fraction of high-angle boundaries decreased in the WM, especially near the UNS32304 side. The fraction of high-angle boundaries in the UNS 43000 and UNS 32304 base metals is 99.57 and 98.7%, respectively. After laser welding, the fraction of high-angle boundaries near the fusion line of UNS 43000 and UNS 32304 decreases to 98.46 and 94.92%, respectively. The fraction of high-, medium- and low-angle boundaries based on the EBSD analysis is shown in Fig. 11.

This increase in the relative fraction of low-angle boundaries is due to the formation of a rapidly solidified as-cast structure. It has been shown that due to the steep temperature gradient and rapid cooling speed in the laser welding process, the solidification process of the molten pool is in a severe nonequilibrium condition which generally produces a high density of low-angle grain boundaries (Ref. 30). Moreover, it has been suggested by



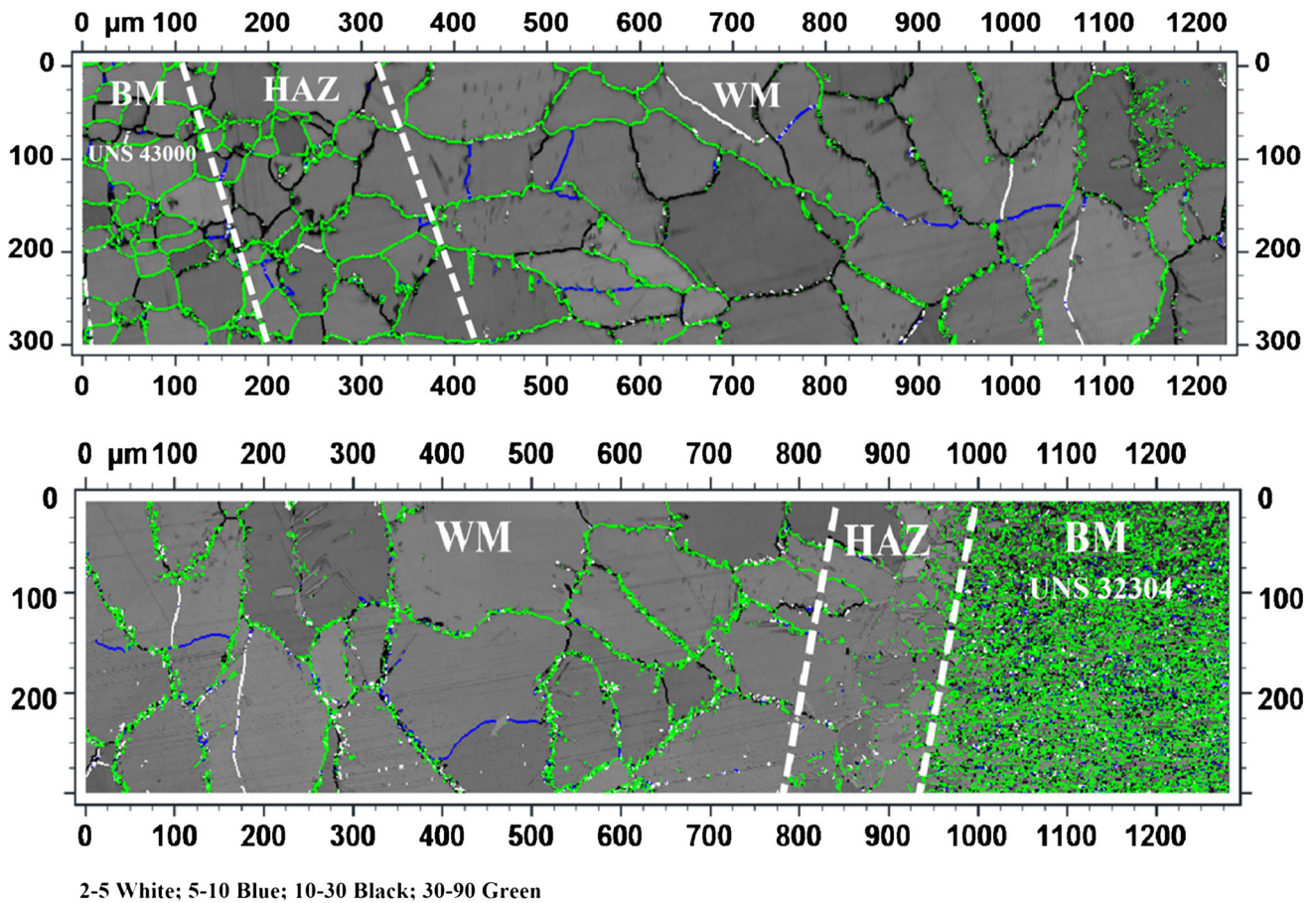


**Fig. 12** The EBSD grain boundary map illustrating the changes in the fraction of low- and high-angle boundaries in a typical welded joint

Jiang et al. (Ref. 31) that the presence of low-angle boundaries was closely associated with the fast heating and cooling rate of the laser welding process. It has been reported that during fusion welding processes such as laser beam, the formation of carbides in the WM is unexpected. But, as already mentioned, some sporadic carbide phases were formed in the WM. It is noteworthy that the Cr-rich carbides and also austenite phase are nucleated mainly from high-angle boundaries.

#### 4. Conclusions

This study investigated microstructure and phase evolutions and also mechanical properties of UNS 43000/UNS32304 joints welded using laser beam welding. Below are the most important findings of the study:

1. A tensile failure occurred from the UNS 43000 BM in the welded sample by full penetration, while by decreasing heat input and the consequent decrease in weld penetration, failure occurred from the WM.
2. The failure mode of the samples welded with the low- and high heat input was ductile while the sample welded with the medium heat input fractured in a brittle mode due to the presence of coarse carbide, particularly  $M_3C$  and  $M_{23}C_6$ . These carbides cause the formation of micro-cracks that propagate across the ferrite matrix.
3. The absence of any solidification crack in the WM confirmed that laser welding with the process parameters and complete mixing of alloying elements is effective.
4. Unlike the results reported by other researchers, no martensitic structure was formed in the WM or in the HAZ despite concentrated heat source in the laser beam welding process.
5. The ratio of  $Cr_{eq}$  to  $Ni_{eq}$  in this study was about 3.7. Accordingly,  $\delta$ -ferrite was the first phase to solidify followed by some transformation from  $\delta$ -ferrite to austenite during cooling. Further, cooling led to the transformation of the austenite phase into  $\alpha$ -ferrite and Cr-rich carbides.
6. The EBSD study showed that the carbide phases formed in different zones were mainly Cr-rich  $M_7C_3$  precipitates.
7. After solidification and in solid-state, the austenite began to precipitate at  $\alpha/\alpha$  grain boundaries named as grain boundary austenite, whereas the Widmanstätten austenite nucleates from the grain boundary austenite in the direction of grain.
8. The analysis of data revealed that the relative fraction of high-angle boundaries in the WM was increased, especially near the UNS32304 side. This increase was attributed to the elimination of cold-worked structure, the formation of migrated grain boundaries during solidification, and finally, a reconstructive transformation, which produced a microstructure composed of ferrite and dispersed carbides with austenite.



## Data Availability

The raw/processed data required to reproduce these findings cannot be shared at this time as the data form a part of an ongoing study.

## Conflict of interest

The authors declare that they have no conflict of interest associated with this publication.

## References

1. T. Teker, Effect of Melt-In and Key-Hole Modes on the Structure and Mechanical Properties of AISI, 430 Steel Welded Using Plasma Transfer Arc Welding, *Phys. Met. Metallogr.*, 2018, **119**, p 669–677. <https://doi.org/10.1134/S0031918X18070116>
2. S. Emami and T. Saeid, A Comparative Study on the Microstructure Development of Friction Stir Welded 304 Austenitic, 430 Ferritic, and 2205 Duplex Stainless Steels, *Mater. Chem. Phys.*, 2019, **237**, p 121833. <https://doi.org/10.1016/j.matchemphys.2019.121833>
3. K.D. Ramkumar, A. Chandrasekhar, A.K. Singh, S. Ahuja, A. Agarwal, N. Arivazhagan, and A.M. Rabel, Comparative Studies on the Weldability, Microstructure and Tensile Properties of Autogeneous TIG Welded AISI, 430 Ferritic Stainless Steel with and Without Flux, *J. Manuf. Process.*, 2015, **20**, p 54–69. <https://doi.org/10.1016/j.jmpro.2015.09.008>
4. M.O.H. Amuda, E.T. Akinlabi, and S. Mridha, Influences of Energy Input and Metal Powder Addition on Carbide Precipitation in AISI, 430 Ferritic Stainless Steel Welds, *Mater. Today Proc.*, 2017, **4**, p 234–243. <https://doi.org/10.1016/j.matpr.2017.01.017>
5. J. Verma, R.V. Taiwade, R. Kataria, and A. Kumar, Welding and Electrochemical Behavior of Ferritic AISI, 430 and Austeno-Ferritic UNS 32205 Dissimilar Welds, *J. Manuf. Process.*, 2018, **34**, p 292–302. <https://doi.org/10.1016/j.jmpro.2018.06.019>
6. A. Claret, S. Sabioni, A. Huntz, E. Conceição, M. Mantel, and C. Haut, Comparative Study of High Temperature Oxidation Behaviour in AISI, 304 and AISI, 439 Stainless Steels, *Mater. Res.*, 2003, **6**, p 179–185
7. G. Sharma, D.K. Dwivedi, and P.K. Jain, Characterization and Strain-Hardening Behavior of Friction Stir-Welded Ferritic Stainless Steel, *J. Mater. Eng. Perform.*, 2017, **26**, p 5997–6005. <https://doi.org/10.1007/s11665-017-3020-0>
8. V.T. Luu, T. Kieu, A. Dinh, H. Das, J. Kim, and S. Hong, Diffusion Enhancement During Electrically Assisted Brazing of Ferritic Stainless Steel Alloys, *Int. J. Precis. Eng. Manuf. Technol.*, 2018, **5**, p 613–621. <https://doi.org/10.1007/s40684-018-0063-0>
9. N. Zhou, R. Lin, and R. Pettersson, Surface Integrity of 2304 Duplex Stainless Steel After Different Grinding Operations, *J. Mater. Process. Tech.*, 2016, **229**, p 294–304. <https://doi.org/10.1016/j.jmatprotec.2015.09.031>
10. J. Kangazian and M. Shamanian, Electron Back Scattered Diffraction Study of Dissimilar Welding Between the Super Duplex Stainless Steel and the Ni—Based Superalloy, *Met. Mater. Int.*, 2019, <https://doi.org/10.1007/s12540-019-00289-0>
11. A. Abdollahi, M. Shamanian, and M.A. Golozar, Comparison of Pulsed and Continuous Current Gas Tungsten Arc Welding in Dissimilar Welding Between UNS S32750 and AISI, 321 in Optimized Condition, *Int. J. Adv. Manuf. Technol.*, 2018, **97**, p 687–696
12. T. Oshima, Y. Habara, and K. Kuroda, Efforts to Save Nickel in Austenitic Stainless Steels, *ISIJ Int.*, 2007, **47**, p 359–364. <https://doi.org/10.2355/isijinternational.47.359>
13. M. Shakil, M. Ahmad, N.H. Tariq, B.A. Hasan, J.I. Akhter, E. Ahmed, M. Mehmood, M.A. Choudhry, and M. Iqbal, Microstructure and Hardness Studies of Electron Beam Welded Inconel 625 and Stainless Steel 304L, *Vacuum*, 2014, **110**, p 121–126. <https://doi.org/10.1016/j.vacuum.2014.08.016>
14. C.-C. Hsieh, X. Guo, C.-M. Chang, and W. Wu, Dendrite Evolution of Delta ( $\delta$ ) Ferrite and Precipitation Behavior of Sigma ( $\sigma$ ) Phase During Multipass Dissimilar Stainless Steels Welding, *Met. Mater. Int.*, 2010, **16**, p 349–356. <https://doi.org/10.1007/s12540-010-0602-x>
15. S. Kou, *Weld. Metall.*, 2003, [https://doi.org/10.1016/0022-4596\(88\)90042-4](https://doi.org/10.1016/0022-4596(88)90042-4)
16. H. Tan, Z. Wang, Y. Jiang, Y. Yang, B. Deng, H. Song, and J. Li, Influence of Welding Thermal Cycles on Microstructure and Pitting Corrosion Resistance of 2304 Duplex Stainless Steels, *Corros. Sci.*, 2012, **55**, p 368–377. <https://doi.org/10.1016/j.corsci.2011.10.039>
17. B. Varbai, T. Pickle, and K. Mäjlinger, Effect of Heat Input and Role of Nitrogen on the Phase Evolution of 2205 Duplex Stainless Steel Weldment, *Int. J. Press. Vessel. Pip.*, 2019, **176**, p 103952. <https://doi.org/10.1016/j.ijpvp.2019.103952>
18. M.O.H. Amuda and S. Mridha, Comparative Evaluation of Grain Refinement in AISI, 430 FSS Welds by Elemental Metal Powder Addition and Cryogenic Cooling, *Mater. Des.*, 2012, **35**, p 609–618. <https://doi.org/10.1016/j.matdes.2011.09.066>
19. G. Mallaiah, A. Kumar, P. Ravinder Reddy, and G. Madhusudhan Reddy, Influence of Grain Refining Elements on Mechanical Properties of AISI, 430 Ferritic Stainless Steel Weldments—Taguchi Approach, *Mater. Des.*, 2012, **36**, p 443–450
20. M.B. Bilgin, C. Meran, and O.E. Canyurt, Optimization of Strength of Friction Stir Welded Joints for AISI, 430 Ferritic Stainless Steels by Genetic Algorithm, *Int. J. Adv. Manuf. Technol.*, 2014, **77**, p 2221–2233. <https://doi.org/10.1007/s00170-014-6590-0>
21. J.C. Lippold, *Welding Metallurgy and Weldability*, Wiley, New Jersey, 2014
22. R. Sołtysiak, T. Giętka, and A. Sołtysiak, The Effect of Laser Welding Power on the Properties of the Joint Made of 1.4462 Duplex Stainless Steel, *Adv. Mech. Eng.*, 2018, <https://doi.org/10.1177/1687814017751949>
23. A.K. Lakshminarayanan and V. Balasubramanian, Evaluation of Microstructure and Mechanical Properties of Laser Beam Welded AISI, 409M Grade Ferritic Stainless Steel, *J. Iron. Steel Res. Int.*, 2012, **19**, p 72–78. [https://doi.org/10.1016/S1006-706X\(12\)60050-8](https://doi.org/10.1016/S1006-706X(12)60050-8)
24. F.J. Humphreys, Review Grain and Subgrain Characterisation by Electron Backscatter Diffraction, *J. Mater. Sci.*, 2001, **36**, p 3833–3854. <https://doi.org/10.1023/A:1017973432592>
25. H. Mostaan, M. Shamanian, S.M. Monirvaghefi, P. Behjati, S. Hasani, M. Fathi Moghaddam, M. Amiri, and J.A. Szpunar, Analysis and Characterization of Microstructural Evolutions, Mechanical Response and Fracture Mechanism of Laser Welded Fe–Co–V Ultra-Thin Foils, *Opt. Laser Technol.*, 2015, **68**, p 211–219. <https://doi.org/10.1016/j.optlastec.2014.12.003>
26. S. Lee, S. Kim, B. Hwang, B.S. Lee, and C.G. Lee, Effect of Carbide Distribution on the Fracture Toughness in the Transition Temperature Region of an SA 508 Steel, *Acta Mater.*, 2002, **50**, p 4755–4762. [https://doi.org/10.1016/S1359-6454\(02\)00313-0](https://doi.org/10.1016/S1359-6454(02)00313-0)
27. M. Abbasi, D.-I. Kim, T.W. Nelson, and M. Abbasi, EBSD and Reconstruction of Pre-transformation Microstructures, Examples and Complexities in Steels, *Mater. Charact.*, 2014, **95**, p 219–231. <https://doi.org/10.1016/j.matchar.2014.06.023>
28. B. Liu, Q. Yang, and Y. Wang, Intereaction and Intermetallic Phase Formation Between Aluminum and Stainless Steel, *Results Phys.*, 2019, **12**, p 514–524. <https://doi.org/10.1016/j.rinp.2018.11.076>
29. D. Arun, K. Devendranath Ramkumar, and R. Vimala, Multi-pass arc Welding techniques of 12 mm Thick Super-Duplex Stainless Steel, *J. Mater. Process. Technol.*, 2019, **271**, p 126–143. <https://doi.org/10.1016/j.jmatprotec.2019.03.031>
30. Z. Jiang, X. Chen, H. Li, Z. Lei, Y. Chen, S. Wu, and Y. Wang, Grain Refinement and Laser Energy Distribution During Laser Oscillating Welding of Invar Alloy, *Mater. Des.*, 2020, **186**, p 108195. <https://doi.org/10.1016/j.matdes.2019.108195>
31. Z. Jiang, W. Tao, K. Yu, C. Tan, Y. Chen, L. Li, and Z. Li, Comparative Study on Fiber Laser Welding of GH3535 Superalloy in Continuous and Pulsed Waves, *Mater. Des.*, 2016, **110**, p 728–739. <https://doi.org/10.1016/j.matdes.2016.08.055>

**Publisher's Note** Springer Nature remains neutral with regard to jurisdictional claims in published maps and institutional affiliations.